

Two-dimensional Radiation-hydrodynamic Model for Supercritical Disk Accretion Flows onto Neutron Stars

Ken OHSUGA ^{1,2}

¹Department of Physics, Rikkyo University, 3-34-1 Nishi-Ikebukuro, Toshima-ku, Tokyo 171-8501

²Institute of Physical and Chemical Research (RIKEN), 2-1 Hirosawa, Wako, Saitama, 351-0198

(Received 2007 March 7; accepted 2007 June 15)

Abstract

We performed two-dimensional radiation hydrodynamic simulations of supercritical accretion flows around neutron stars (NSs). In contrast with the accretion flows onto black holes (BHs), we find that the shell-shaped high-density regions form around the NSs, since the radiation force is enhanced in the innermost regions. The enhanced radiation force drives strong outflows above and below the disk. The mass-accretion rate onto the NS exceeds the critical rate, L_E/c^2 , with L_E being the Eddington luminosity. However it is about 20–30% of that onto the BH, under the condition that we employ the same mass-input rate, \dot{M}_{input} , which is mass injected from the outer disk boundary per unit time. The mass-outflow rate is a few-times larger in flows around NSs than in flows around BHs. The supercritical NS accretion flows mainly release the accretion energy as the kinetic energy of the outflows, though the disk luminosity is predominant over the kinetic energy output rate in the BH accretion flows. The resulting velocity and mass-outflow rate of the outflows are $0.2–0.3c$ and $150–700L_E/c^2$, respectively, for the mass-input rate of $3 \times 10^2 \lesssim \dot{M}_{\text{input}}/(L_E/c^2) \lesssim 3 \times 10^3$. This implies that the SS433 jets can be roughly explained by the supercritical accretion onto a NS. However, the collimation angle of the outflows in our simulations ($\sim 20^\circ$) is larger than that of the SS433 jets (a few degrees).

Key words: accretion, accretion disks — ISM: jets and outflows — hydrodynamics — stars: neutron — stars: individual (SS433)

1. INTRODUCTION

Luminous compact objects are thought to be powered by accretion flows. It is widely believed that accretion processes can be basically described by the standard disk model, proposed by Shakura & Sunyaev (1973). However, this model breaks down if the mass-accretion rate is comparable to, or exceeds, the critical rate, L_E/c^2 , where L_E is the Eddington luminosity. Then, advective cooling is predominant over radiative cooling.

Abramowicz et al. (1988) established the slim-disk model, which is one-dimensional model that includes the advective cooling. Two-dimensional radiation-hydrodynamic (RHD) simulations of supercritical accretion flows around black holes (BHs) were attempted by Eggum, Coroniti, & Katz (1988) and Okuda (2002). By performing long-term two-dimensional RHD simulations, we have for the first time confirmed the occurrence of supercritical disk accretion onto BHs (Ohsuga et al. 2005, hereafter Paper I).

In the case of the supercritical disk accretion flows around BHs, a large amount of photons generated inside the disk are swallowed by the BH with accreting matter. This effect largely attenuates the radiation force, assisting the occurrence of inflow motion. However, the situation considerably differs in disks around neutron stars (NSs). In this case, the radiation energy is not swallowed by the NS, and the energy of accreting matter would be converted

to radiation energy at the NS surface. Thus, the radiation force is enhanced and works to prevent the inflow motion, although the matter is accelerated inward by the radiation force in cooperation with the gravity at the very vicinity of the BH.

The X-ray source SS433 exhibits powerful relativistic jets. The observations of Doppler-shifted iron lines revealed that the mass-outflow rate of the jets highly exceeds the critical rate for the NS/stellar BH (Kotani et al. 1996). Thus, SS433 is thought to undergo supercritical accretion flows, although its central object is still not understood. Whereas some researchers have suggested that a BH exists in SS433, a NS hypothesis is not denied. On the other hand, by the X-ray observations of low-mass X-ray binaries (LMXBs), Takahashi & Makishima (2006) recently discovered a sign of supercritical accretion onto the NSs. They reported that the spectra of LMXBs consist of three components in the supercritical phase. Two components are thought to be emission of the disk and the NS surface, which are observed when the X-ray luminosity is much smaller than the Eddington luminosity as well. The third component appears only in the supercritical phase, and is thus presumably the emission of outflows driven by the strong radiation force of the supercritical accretion disks.

The super or near-critical accretion onto NS has been studied in spherical geometry by analytic method and numerical calculations (Burger & Katz 1980, 1983; Klein

et al. 1980; Miller 1990). They reported the maximum accretion rate to be about critical late and the maximum luminosity to be near the Eddington luminosity. However, Demmel et al. (1990) proposed a inhomogeneous spherical accretion model, by which the luminosity can exceed the Eddington luminosity for large mass-accretion rate. The maximum luminosity of supercritical disks around a magnetized NS was suggested to be $46L_E$ by Lipunov (1982). Two-dimensional RHD simulations of supercritical accretion flows around NSs were attempted by Okuda & Fujita (2000). However, though the matter was injected at the supercritical rate from the outer boundary, most of the matter was blown off from the system as the jets and the disk wind. The steady structure and physical properties of supercritical disk accretion onto a NS is still open issue.

In this paper, we consider the supercritical disk accretion flows around non-magnetic and non-rotating NSs, based on long-term two-dimensional RHD simulations. We also compare them with supercritical BH accretion flows. In §2, our model and numerical method are described. We present the numerical results in §3. §4 and §5 are devoted to discussion and conclusions.

2. MODEL AND METHOD

2.1. Basic Equations

We describe the RHD equations including the viscosity term. We use spherical polar coordinates (r, θ, φ) , where r is the radial distance, θ is the polar angle, and φ is the azimuthal angle. The origin is set at the central object (NS otherwise BH). In the present study, we assume axisymmetry with respect to the rotation axis (i.e., $\partial/\partial\varphi = 0$), as well as reflection symmetry relative to the equatorial plane (with $\theta = \pi/2$). We describe the gravitational field of the central object in terms of pseudo-Newtonian hydrodynamics, in which the gravitational potential is given by $-GM/(r - r_S)$ as was introduced by Paczynsky & Wiita (1980), where M is the mass of the central object and $r_S = 2GM/c^2$ is the Schwarzschild radius. The flow is assumed to be non-self-gravitating. The basic equations are the continuity equation,

$$\frac{\partial \rho}{\partial t} + \nabla \cdot (\rho \mathbf{v}) = 0, \quad (1)$$

the equations of motion,

$$\begin{aligned} \frac{\partial(\rho v_r)}{\partial t} + \nabla \cdot (\rho v_r \mathbf{v}) &= -\frac{\partial p}{\partial r} + \rho \left\{ \frac{v_\theta^2}{r} + \frac{v_\varphi^2}{r} - \frac{GM}{(r - r_S)^2} \right\} + f_r + q_r, \quad (2) \\ \frac{\partial(\rho r v_\theta)}{\partial t} + \nabla \cdot (\rho r v_\theta \mathbf{v}) &= -\frac{\partial p}{\partial \theta} + \rho v_\varphi^2 \cot \theta + r f_\theta + r q_\theta, \quad (3) \\ \frac{\partial(\rho r v_\varphi \sin \theta)}{\partial t} + \nabla \cdot (\rho r v_\varphi \sin \theta \mathbf{v}) &= r q_\varphi \sin \theta, \quad (4) \end{aligned}$$

the energy equation of the gas,

$$\frac{\partial e}{\partial t} + \nabla \cdot (e \mathbf{v}) = -p \nabla \cdot \mathbf{v} - 4\pi \kappa B + c \kappa E_0 + \Phi_{\text{vis}}, \quad (5)$$

and the energy equation of the radiation,

$$\frac{\partial E_0}{\partial t} + \nabla \cdot (E_0 \mathbf{v}) = -\nabla \cdot \mathbf{F}_0 - \nabla \mathbf{v} : \mathbf{P}_0 + 4\pi \kappa B - c \kappa E_0. \quad (6)$$

Here, ρ is the mass density, $\mathbf{v} = (v_r, v_\theta, v_\varphi)$ is the velocity, p is the gas pressure, e is the internal energy density of the gas, B is the blackbody intensity, E_0 is the radiation energy density, \mathbf{F}_0 is the radiative flux, \mathbf{P}_0 is the radiation pressure tensor, κ is the absorption opacity, $\mathbf{q} = (q_r, q_\theta, q_\varphi)$ is the viscous force, and Φ_{vis} is the viscous dissipative function, respectively. The radiation force $\mathbf{f}_{\text{rad}} = (f_r, f_\theta)$ is given by

$$\mathbf{f}_{\text{rad}} = \frac{\chi}{c} \mathbf{F}_0, \quad (7)$$

where $\chi (= \kappa + \rho \sigma_T / m_p)$ is the total opacity with σ_T being the Thomson-scattering cross-section and m_p being the proton mass.

As the equation of state, we use

$$p = (\gamma - 1)e, \quad (8)$$

where γ is the specific heat ratio. The temperature of the gas, T , can then be calculated from

$$p = \frac{\rho k T}{\mu m_p}, \quad (9)$$

where k is the Boltzmann constant and μ is the mean molecular weight.

The radiative flux and the radiation stress tensor are solved under the flux-limited diffusion approximation, so that they are expressed in terms of the radiation energy density (Levermore & Pomraning 1981). It gives correct relations in the optically thick diffusion limit and optically thin streaming limit, respectively.

We assume that the only $r\varphi$ -component of the viscous stress tensor, which plays important roles for the transport of the angular momentum and heating of the disk plasma, is non zero,

$$\tau_{r\varphi} = \eta r \frac{\partial}{\partial r} \left(\frac{v_\varphi}{r} \right), \quad (10)$$

where η is the dynamical viscosity coefficient. Then, the radial and polar components of the viscous force are null ($q_r = q_\theta = 0$), and the right hand side of equation (4) is described as

$$r q_\varphi \sin \theta = \frac{1}{r^2} \frac{\partial}{\partial r} (r^3 \tau_{r\varphi} \sin \theta). \quad (11)$$

The viscous dissipative function is given by

$$\Phi_{\text{vis}} = \eta \left[r \frac{\partial}{\partial r} \left(\frac{v_\varphi}{r} \right) \right]^2. \quad (12)$$

The dynamical viscosity coefficient is prescribed as

$$\eta = \alpha \frac{p + \lambda E_0}{\Omega_K}, \quad (13)$$

where α is the viscosity parameter, and Ω_K is the Keplerian angular speed. Here, the parameter, λ , is given by $(2 + \mathcal{R})/(6 + 3\mathcal{R} + \mathcal{R}^2)$, using the dimensionless quantity, $\mathcal{R} = |\nabla E_0| / (\chi E_0)$. Since it becomes $1/3$ in the

optically thick regime and vanishes in the optically thin regime, the viscous stress tensor is related to the gas pressure or the total pressure, p_{total} , as,

$$\tau_{r\varphi} \propto \begin{cases} \alpha p_{\text{total}} & (\text{optically thick limit}) \\ \alpha p & (\text{optically thin limit}) \end{cases} . \quad (14)$$

It is modified α prescription of the viscosity, which was proposed by Shakura & Sunyaev (1973).

2.2. Numerical Method

We numerically solved the set of RHD equations using an explicit-implicit finite-difference scheme on the Eulerian grids. Our methods were similar to those of Paper I, but we used the explicit scheme for solving the radiative flux term in equation (6), and employ constant time step (Ohsuga 2006). The computational domain consisted of spherical shells of $2.4r_{\text{S}} \leq r \leq 500r_{\text{S}}$ and $0 \leq \theta \leq 0.5\pi$, which were divided into 96×96 grid cells.

We employed two types of inner-boundary conditions for the accretion flows around the NSs (NS model) and the BHs (BH model). The radial component of the radiative flux is given by

$$F_0^r = -cE_0, \quad (15)$$

at the inner boundary for the BH model. This means that the radiative flux term always contribute to transport of the radiation energy onto the BH ($F_0^r < 0$). In addition, because of the inflow motion at the inner boundary ($v_r < 0$), the radiation energy and the gas energy are swallowed by the BH via advection, $v_r E_0 < 0$ and $(e + \rho v^2/2)v_r < 0$, in our simulations. In other words, the BH always swallows both the matter and the energy. In contrast, we assumed that the NS cannot swallow the energy. The gas energy advected onto the NS surface is supposed to be immediately released as the radiation. Hence, we set

$$F_0^r = -ev_r - \frac{1}{2}\rho v^2 v_r, \quad (16)$$

at the inner boundary for the NS model. Our simulations gave negative radial velocity at the inner boundary ($v_r < 0$), leading an outward radiative flux ($F_0^r > 0$) at the NS surface. When we updated the radiation energy density by solving the equation (6), the advective term of the radiation energy was numerically set to be null at the inner boundary, $v_r E_0 = 0$, whereas the radial velocity and the radiation energy density are both non zero there. To sum up, the matter accretes onto the NS surface, but the energies of radiation and gas were not swallowed by the NS in our simulations.

We employed a no-torque condition at the surface of the BH. Thus, the viscosity does not work at the inner boundary in the case of the BH accretion flows. In contrast, we assumed that the viscosity works even at the very vicinity of the inner boundary in the NS model. Therefore, the rotation energy of the gas is effectively dissipated and converted to radiation energy near the NS surface. This viscous effect at the inner boundary would depend on the rotation velocity of the NS. However, we note that our results do not change so much unless the rotation velocity

of the NS surface is comparable to the Keplerian velocity.

The radiation energy density increases near the NS surface because of such inner-boundary conditions, leading the enhanced radiation force. The radiation force counteracts with the gravity and works to prevent the inflow motion. In contrast, the matter is accelerated inward by the radiation force in cooperation with the gravity in the case of the BH model.

We started the calculations with a hot, rarefied, and optically thin atmosphere. There was no cold dense disk in the computational domain, initially. Matter was continuously injected into the computational domain through the outer disk boundary ($r = 500r_{\text{S}}$, $0.45\pi \leq \theta \leq 0.5\pi$). Therefore, we could avoid any influence of the initial configuration on the final result, although a long integration time is required. The injected matter is supposed to have a specific angular momentum corresponding to the Keplerian angular momentum at $r = 100r_{\text{S}}$. We set the mass-input rate, \dot{M}_{input} , which is the mass injected into the computational domain per unit time, so as to be constant at the outer disk boundary. At the outer boundary region above the outer disk boundary ($r = 500r_{\text{S}}$, $\theta < 0.45\pi$), we used free boundary conditions and allowed for matter to go out but not to come in.

Throughout the present study, we assume $\alpha = 0.1$, $\gamma = 5/3$, $\mu = 0.5$, and $M = 1.4M_{\odot}$. Thus, the radius of the inner boundary, $2.4r_{\text{S}}$, is nearly 10km. Such mass and the radius are consistent with recent models of a NS, although they slightly depends on the equation of state inside the NS. Since we aim to understand any differences of the accretion flows around NSs and BHs, the mass of the BH was also set to be $1.4M_{\odot}$. For the absorption opacity, we considered free-free absorption and bound-free absorption for solar metallicity (Hayashi, Hoshi, & Sugimoto 1962; Rybicki & Lightman 1979)

3. RESULTS

3.1. Quasi-steady Structure

We first give a brief overview of the time evolution of our simulations. The overall evolution of the NS accretion flows is similar to that of the BH accretion flows (see Paper I in detail). It is divided into two distinct phases: an accumulation phase and a quasi-steady phase. Because the injected matter has a small specific angular momentum, it firstly free falls, but accumulates around regions with a radius of $r \sim 100r_{\text{S}}$, forming a rotating disk (accumulation phase). Eventually, the viscosity starts to work. The angular momentum of the gas is transported outward, driving the inflow motion (quasi-steady phase). Radiatively driven outflow is generated around the rotation axis in this phase. The critical time separating these two phases roughly coincides with the viscous timescale.

Figure 1 indicates time-averaged contours of the density in the quasi-steady state for the NS model (the upper-left panel) and the BH model (the upper-right panel), where we adopt $\dot{M}_{\text{input}} = 10^3 L_{\text{E}}/c^2$. As shown in these panels, a high-density region appears around the equatorial plane (yellow) and a rarefied region forms near the rota-

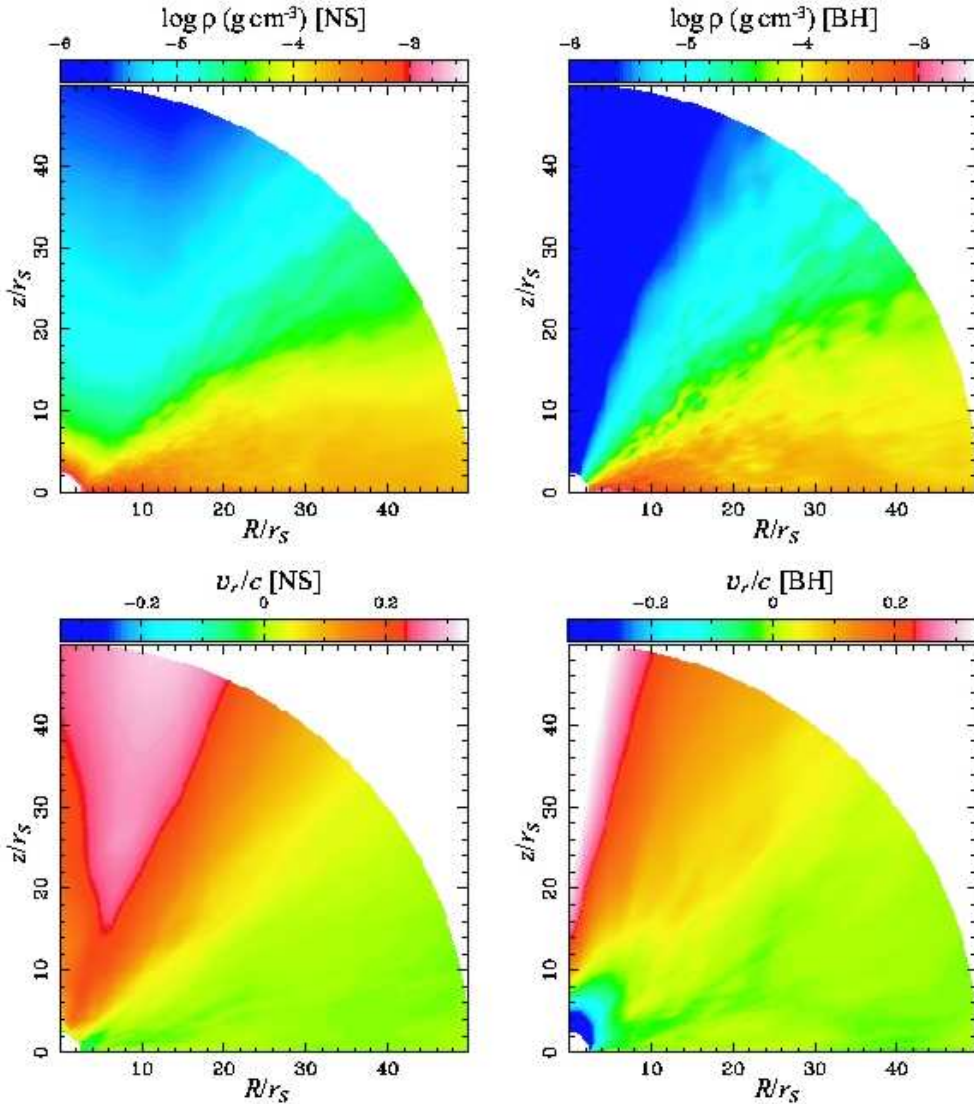


Fig. 1. Time-averaged distributions of the density (the upper-left panel) and the radial velocity normalized by the speed of light (the lower-left panel) on the R - z plane for the NS model. Those for the BH model are shown in the upper-right and lower-right panels. The adopted parameter is $\dot{M}_{\text{input}} = 10^3 L_{\text{E}}/c^2$.

tion axis (blue) in both models. The high-density regions indicate the radiation pressure-supported disks. The radiation force drives the outflow in the less-dense region above the disk. We find a significant difference in the very vicinity of the inner boundary. Although the rarefied region connects to the inner boundary along the rotation axis in the BH model, the high-density region (orange) surrounds the NS.

Such a shell-shaped structure is built up by the radiation force, which counteracts with the gravity. Since the radiation energy, as well as the gas energy, is not swallowed by the NS in our simulations, the radiation energy increases near the inner boundary. Hence, the radial component of the radiative flux becomes positive (outward flux) there, so that the radiation force works to prevent the inflow motion (discussed later). Here, we note that such a difference in the density distribution would affect

the emergent spectra and its viewing-angle dependence. We discuss this point in §3.4.

In the lower-left (NS model) and lower-right (BH model) panels, we display the radial velocity normalized by the speed of light. It is found that the gas slowly falls inward in the dense disk regions. On the other hand, the matter is accelerated outward in the rarefied region above the disk, except for the very vicinity of the BH, where the gas falls onto the BH. We find in the NS model that the typical velocity of the outflow is $0.2 - 0.3c$ and its collimation angle is $\sim 20^\circ$. The BH model exhibits more collimated high velocity regions along the rotation axis. The supercritical accretion onto the NS forms more powerful outflows than does that around the BH. Both the mass-outflow rate and the kinetic energy output rate by the outflow are larger in the NS model than in the BH model (discussed later).

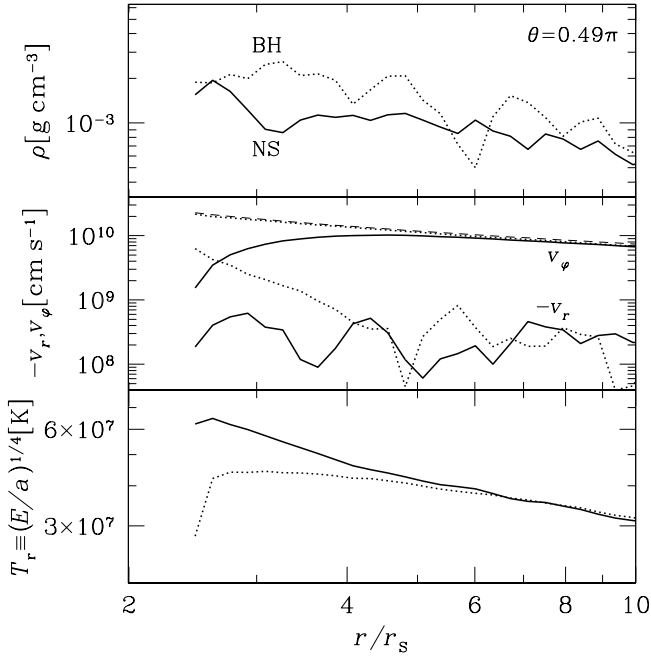


Fig. 2. Time-averaged one-dimensional profiles of the density (the top panel), the radial and rotation velocities (the middle panel), and the radiation temperature (the bottom panel) near the equatorial plane, $\theta = 0.49\pi$. The solid and dotted lines indicate the results of the NS model and the BH model, respectively. The Keplerian velocity is represented by the dashed line in the middle panel, which almost overlaps with upper dotted line. The adopted parameter is $M_{\text{input}} = 10^3 L_E/c^2$.

In Figure 2 we represent one-dimensional distributions of the gas density (the top panel), the inflow and rotation velocities (the middle panel), and the radiation temperature (the bottom panel) near the equatorial plane, $\theta = 0.49\pi$. Here, the solid and dotted lines indicate the results of the NS model and the BH model, respectively. The radiation temperature is defined as $T_r \equiv (E_0/a)^{1/4}$, where a is the radiation constant. As shown in the top panel, the gas density in the NS model is comparable to, or slightly smaller than, that in the BH model. It is found in the middle and bottom panels that there are significant differences in the profiles of the velocities and the radiation temperature between two models. These are induced by the differences in the inner-boundary conditions.

In the present simulations, the viscosity worked even at the inner boundary for the NS model, whereas we used no-torque condition at the surface of the BH. Therefore, the rotation velocity deviates from the Keplerian velocity as the flow approaches the NS, though the gas rotates at about the Keplerian velocity in the regions of $r \gtrsim 5r_s$ (see the middle panel). In contrast, the rotation velocity of the BH model roughly agrees with the Keplerian velocity even in the vicinity of the inner boundary.

We find in the bottom panel that the radiation energy is larger in the NS model than in the BH model near the inner boundary. Near the surface of the NS, the viscosity effectively converts the rotation energy into the internal

energy of the gas. Subsequently, the gas-radiation interaction turns such energy into the radiation energy. In addition, the energy of the gas falling onto the NS is converted to radiation energy at the surface of the NS (see equation [16]). Due to the combination of these effects, the radiation energy increases around the inner boundary in the NS model. In the case of the BH accretion flow, the no-torque condition is employed and the energy is swallowed by the BH, attenuating the radiation energy density around the inner boundary.

We find in the middle panel that the resulting inflow velocity, $-v_r$, in the NS model is much smaller than that in the BH accretion flows around the inner boundary. The radiation force is enhanced in the vicinity of the NS surface via the large radiation energy and its steep profile (see the bottom panel). Thus, the radiation force works to decelerate the inflow motion. That radiative deceleration in the supercritical flows around the NS was mentioned by Burger & Katz (1980; 1983). In the BH model, the radiative deceleration is relatively inefficient, since the flatter profile of the radiation energy density leads to a small radiative flux (see the bottom panel). In addition, the radiation force accelerates the gas inward in cooperation with the gravity at the surface of the BH, since the radial component of the radiative flux is negative (inward flux). As a result, the inflow velocity increases as the flow approaches the BH.

3.2. Mass Accretion Rate and Mass Outflow Rate

We plot in Figure 3 the mass-accretion rate onto the NS/BH (*circles*) and the mass-outflow rate (*squares*) normalized by the critical accretion rate as functions of the mass-input rate. Here, the mass-outflow rate is the mass ejected through the outer boundary per unit time by the high-velocity outflow whose radial velocity exceeds the escape velocity. The filled and open symbols indicate the results of the NS and BH models, respectively.

We find that both the mass-accretion rate and the mass-outflow rate increase with an increase of the mass-input rate. We find that the supercritical accretion is not a peculiar phenomenon in BH accretion flows. The mass-accretion rate of the NS model highly exceeds the critical accretion rate, although it is as small as 20–30% for the BH model. Especially surprising is that the mass-outflow rate for the NS model exceeds that in the case of BH accretion flows, although the mass-accretion rate is much smaller in the NS model than in the BH model. The supercritical disk around NS blows away a few times as much matter as outflowing matter of the disk around the BH. The supercritical accretion flows around the NSs effectively produce the radiatively driven outflow. We discuss this point again in the next subsection.

3.3. Luminosity and Kinetic Energy Output Rate

In Figure 4 we represent the luminosity and the kinetic energy output rate as functions of the mass-accretion rate onto the NS/BH, \dot{M}_{acc} . The filled (open) circles and squares indicate the luminosity, L_{rad} , and the kinetic energy output rate, L_{kin} , for NS (BH) model. Here, the

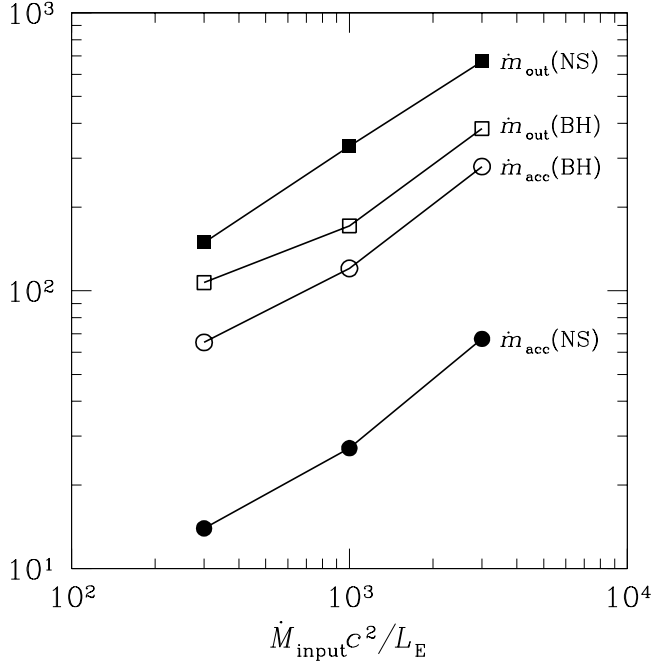


Fig. 3. Mass-accretion rate onto the NS/BH and mass-outflow rate by the high velocity outflows normalized by the critical rate, \dot{m}_{acc} (circles) and \dot{m}_{out} (squares), as functions of normalized mass-input rate. The filled and open symbols indicate the results of the NS model and the BH model, respectively.

luminosity is evaluated by integrating the radiative flux at the outer boundary. The kinetic energy output rate is the kinetic energy ejected through the outer boundary per unit time by the high-velocity outflow. The luminosity of the NS, L_{NS} , which is evaluated by integrating the radiative flux at the inner boundary (see equation [16]), is represented by the triangles. The mass-input rate is set to be $\dot{M}_{\text{input}}/(L_E/c^2) = 3 \times 10^2, 10^3$, and 3×10^3 from left to right.

We find in this figure that the luminosity and the kinetic energy output rate increase with an increase of the mass-accretion rate in both models. It is also found that the energy conversion efficiency, $(L_{\text{rad}} + L_{\text{kin}})/\dot{M}_{\text{acc}}c^2$, of the NS accretion flows is by one order of magnitude larger than that of the BH accretion flows. For instance, when the mass-accretion rate is around $70L_E/c^2$, we find $L_{\text{rad}} \sim 9L_E$ and $L_{\text{kin}} \sim 19L_E$ for the NS model and $L_{\text{rad}} \sim 2L_E$ and $L_{\text{kin}} \sim L_E$ for the BH model. The sum of the luminosity and the kinetic energy output rate almost equals the accretion energy for the NS model, $L_{\text{rad}} + L_{\text{kin}} \sim GM\dot{M}_{\text{acc}}/(2.4r_S - r_S)$. In contrast, we find $L_{\text{rad}} + L_{\text{kin}} \ll GM\dot{M}_{\text{acc}}/(2.4r_S - r_S)$ in the BH model. This is natural since, unlike a BH, a NS neither swallow the radiation energy nor the gas energy in the present study.

In Figure 4 we find $L_{\text{rad}} > L_{\text{kin}}$ for the BH model, but $L_{\text{rad}} < L_{\text{kin}}$ for the NS model. The radiation force is enhanced via the inner-boundary conditions for the NS model, whereby the rotation energy is converted to radiation energy via the viscosity and the energy of the in-

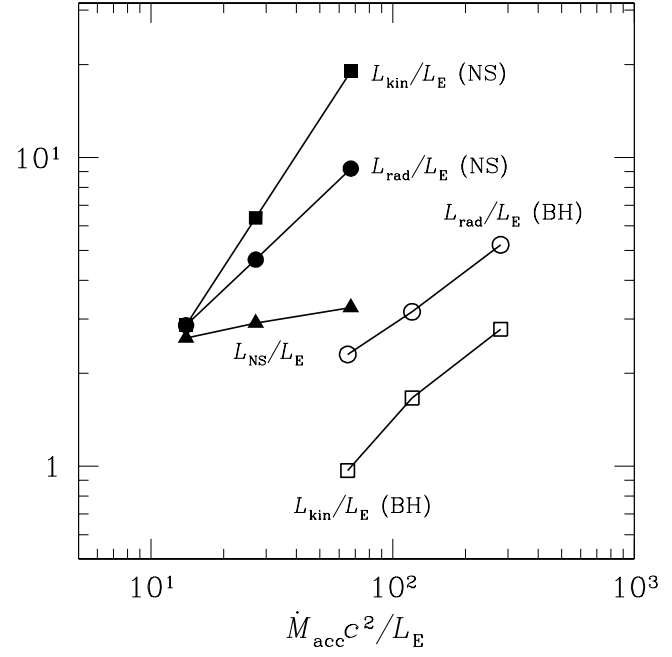


Fig. 4. Luminosity (circles) and kinetic energy output rate (squares) as functions of normalized mass-accretion rate onto the central object, $\dot{M}_{\text{acc}}c^2/L_E$, for $\dot{M}_{\text{input}}c^2/L_E = 3 \times 10^2, 10^3, 3 \times 10^3$ from left to right. The filled and open symbols indicate the results of the NS model and the BH model, respectively. The luminosity of the NS is represented by the filled triangles.

flowing matter is also converted to the radiation energy without being swallowed by the NS, driving the strong radiatively driven outflow.

Next, we explain the reason why the mass-accretion rate onto the NS can be over the critical rate, L_E/c^2 . In the present simulations, the luminosity of the NS corresponds to the energy of the accreting gas per unit time (see equation [16]). Thus, if the gas sufficiently releases its energy before reaching the inner boundary, the gravity is predominant over the radiation force at the NS surface, allowing the accreting motion. Otherwise, the radiation force would prevent the inflow motion at the inner boundary. Due to such mechanism, the resulting luminosity of the NS is self-regulated so as to meet the condition that the radiation force does not exceed the gravity. Since we employ the pseudo-Newtonian potential, the critical luminosity, in which the radiation force balances with the gravity, is $\sim 3L_E$. To conclude, although the energy transported onto the NS surface per unit time is limited to be $\sim 3L_E$, the mass-accretion rate can greatly exceed the critical rate, as long as the matter sufficiently loses its energy before reaching the NS surface. Since the BH can swallow the gas energy, as well as the radiation energy, the mass-accretion rate can exceed the critical rate even if the matter has a large amount of the energy.

3.4. Effective Temperature Profile

Finally, we consider the effective temperature by solving radiation transfer, and represent its profiles for the incli-

nation angles of $i = 0, \pi/12$, and $\pi/6$ in Figure 5. Here, X is the horizontal coordinate on the observer's screen. The adopted parameter is $\dot{M}_{\text{input}} = 10^3 L_E/c^2$. Then, the luminosity is $\sim 5L_E$ for the NS model and $\sim 3L_E$ for the BH model. In this subsection, we focus on the effective-temperature profile and its viewing-angle dependence.

This figure shows that the maximal effective temperature is not very sensitive to the viewing angle for the NS model. It merely varies from $3 \times 10^6 \text{ K}$ to $5 \times 10^6 \text{ K}$. In contrast, it shifts from $2 \times 10^6 \text{ K}$ to $9 \times 10^6 \text{ K}$ for the BH model. We also find that the accretion flow around the NS exhibits a flatter profile of the effective temperature, even in the face-on view.

As shown in the Figure 1, the density distribution is more anisotropic in the BH model than in the NS model (note that the outflow region above the disk is relatively dense in the NS model, as compared with the BH model). In addition, a high-density shell forms only in the NS model. Due to such enhanced anisotropy of the density distribution, the emission of the BH model is more collimated in the polar direction than that of the NS model, producing the steeper effective-temperature profile in the face-on view (see also Paper I). In contrast, the effective-temperature profile becomes almost flat in the NS model.

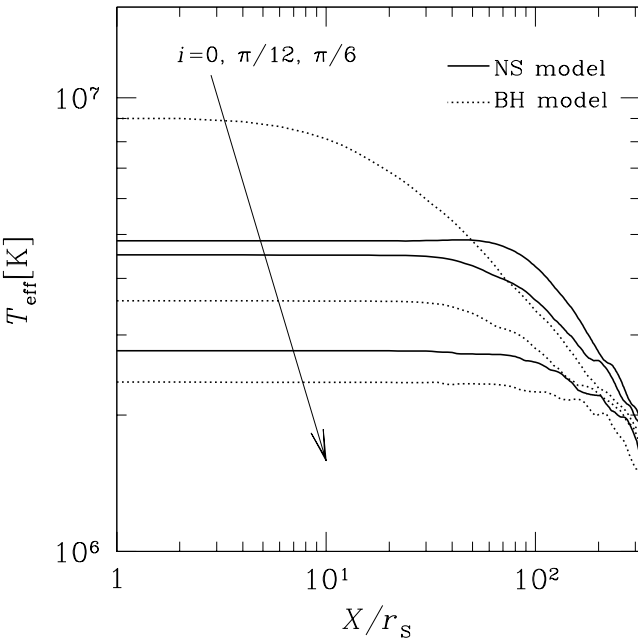


Fig. 5. Effective-temperature profiles in the X -directions for the viewing angle of $i = 0, \pi/12$, and $\pi/6$. Here, X is the horizontal coordinate on the observer's screen. The solid and dotted lines represent the results of NS model and BH model, respectively.

4. DISCUSSION

4.1. Comparison with SS433 jets

By the present simulations, we showed that the relativistic outflows appear above and below the supercritical

disk. Here, we compare the simulated outflows of the NS model with the jets of SS433.

Based on the observations of the Doppler-shifted ion lines, Kotani et al. (1996) reported the mass-outflow rate of the SS433 jets to be $> 5 \times 10^{-7} M_\odot \text{ yr}^{-1}$, probably $2 \times 10^{-6} M_\odot \text{ yr}^{-1}$. Since these values correspond to $> 1.7 \times 10^2 L_E/c^2$ and $6.7 \times 10^2 L_E/c^2$ for the mass of $1.4M_\odot$, our NS model can explain the mass-outflow rate of the SS433 jets, if the mass-input rate is within the range $3 \times 10^2 \lesssim \dot{M}_{\text{input}}/(L_E/c^2) \lesssim 3 \times 10^3$. The typical velocity of the outflows, $(2L_{\text{kin}}/\dot{m}_{\text{out}} L_E)^{1/2} c$, is $0.2 - 0.3c$. It nicely agrees with the velocity of $0.26c$ observed in SS433.

However, the collimation angle of the jets of our model deviates from that of the SS433 jets. The collimation angle of the SS433 jets seems to be as small as a few degrees. However, we find the angle of $\sim 20^\circ$ in our simulations (see the upper-left panel in Fig. 1). The magnetic effects might resolve this issue. Kato, Hayashi, & Matsumoto (2004) have reported that the collimated jets are produced via a magnetic interaction between a weakly magnetized NS and its accretion disk. The jets might be collimated at the outer region, although the size of the computational domain was restricted to $500r_S$ in the present study. We will clarify this point in future work by performing the simulations with larger computational domains.

We next discuss about the density and the temperature. Kotani et al. (1996) also estimated the density and the temperature in the X-ray emitting region, $r \gtrsim 10^9 \text{ cm}$ ($2 \times 10^3 r_S$ for the mass of $1.4M_\odot$), as $\rho < 10^{-8} \text{ g cm}^{-3}$ and $T \sim 3 \times 10^8 \text{ K}$. In Figure 6 we represent the resulting profiles of the density (the top panel) and the temperature (the bottom panel) near the rotation axis, $\theta = 4^\circ$ for $\dot{M}_{\text{input}} = 10^3 L_E/c^2$. As shown in this figure, the density and the temperature are roughly proportional to r^{-1} and $r^{-2/3}$, respectively. Thus, our results are roughly consistent with the observations as long as the slope of the profiles does not drastically change up to the regions of $r \sim 2 \times 10^3 r_S$, although our computational domain does not cover the X-ray emitting region. We need the numerical simulations with larger computational domains.

The density and the temperature of the SS433 jets near the compact object are investigated by Inoue et al. (2001). They analytically studied and reported $\rho \sim 7 \times 10^{-7} \text{ g cm}^{-3}$ at $r \sim 9 \times 10^7 \text{ cm}$. Since this size corresponds to $r \sim 2 \times 10^2 r_S$ for a mass of $1.4M_\odot$, their result roughly agrees with our result (see the top panel). On the other hand, whereas we used the one-temperature assumption in the present simulations, it is not guaranteed in the outflow regions. This is because the equipartition time, $\lesssim 10^{-3} \text{ s}$, is comparable to, or larger than, the escape time at the regions of $r \lesssim 200r_S$. In the case in which the one-temperature assumption breaks down, the ion temperature would be much higher than the electron temperature. Such a tendency was also reported by Inoue et al. (2001). In their work, the ion temperature was one order of magnitude higher than the electron temperature. However, their model predicts a much higher electron temperature, $\sim 2 \times 10^{10} \text{ K}$, than the result of our model,

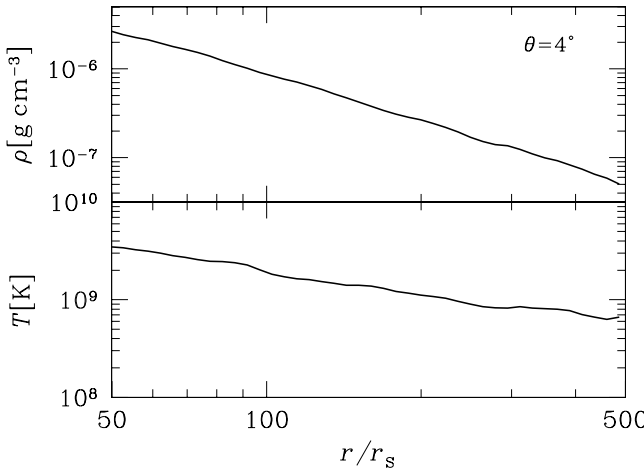


Fig. 6. Time-averaged one-dimensional profiles of the density (the top panel) and the gas temperature (the bottom panel) in the outflow regions ($\theta = 4^\circ$) for the NS model.

$\sim 10^9$ K. Although we solved a set of RHD equations in the present simulations, Inoue et al. (2001) investigated the only the energetics by assuming the dynamics and the shape of the jets. We should perform RHD simulations, in which the ion and electron temperatures are separately treated.

4.2. Future work

We need to calculate the spectra and compare them with the results of the observations for detailed study. A symptom of the supercritical accretion onto NSs has been discovered by the X-ray observations. Takahashi & Makishima (2006) reported that the LMXB spectra can be understood by the superposition of emissions from an accretion disk, the NS surface, and outflows. Since the emission, which is thought to come from the outflows, is not detected in the subcritical phase, they concluded that the outflows are accelerated by the strong radiation force of the supercritical accretion flows. By solving the monochromatic radiation-transfer equation, we calculated the effective-temperature profiles, and show them in Figure 5. However, the emergent spectra of the supercritical accretion flows are not a simple superposition of blackbody spectra with various effective temperatures (Ohsuga, Mineshige, & Watarai 2003). In addition, the inverse Compton scattering would also contribute to the spectra, though it is not included in our simulations. A detailed study of the emergent spectra should be explored in future work.

In the present study, we consider the accretion flows around non-rotating NSs. Our results do not change that much as long as the rotation velocity of the NS surface is much smaller than the Keplerian velocity. Here, we note that the spin-up timescale of the NSs by mass accretion, $\sim 10^8$ yr, is much longer than the integration time of the present simulation, ~ 10 s. The rapidly rotating NSs seem to exist in the LMXBs, since they are thought to be progenitors of millisecond radio pulsars (Backer et

al. 1982; Wijnands & van der Klis 1998). The rapid rotation plays important roles in the disk structure and the temperature profile via modification of the space-time geometry (Bhattacharyya et al. 2000, 2001a, b). A detailed consideration of the disks around the rapidly rotating NSs, however, beyond the scope of this paper.

We consider the non-magnetized NSs in the present study. If the NSs have strong magnetic fields, the flow structure might drastically change (Kato et al. 2001; Koldoba et al. 2002; Romanova et al. 2003). In addition, the source of the disk viscosity is likely to be of magnetic origin, though we used the α -prescription of the viscosity (Hawley, Balbus, & Stone 2001; Machida, Matsumoto, & Mineshige 2001; Balbus 2003, for a review). We need radiation magnetohydrodynamic (MHD) simulations. Local radiation MHD simulations of the accretion flow have been performed by Turner et al. (2003) and Turner (2004). Furthermore, we should include the synchrotron self-Compton processes. It is important to separately treat the ion temperature and the electron temperature. As we discussed in §4.1, the one-temperature assumption might break down in the outflow regions because of low density and high velocity. The radiation MHD simulations are required again for such a study.

Although the matter did not lose angular momentum by the gas-radiation interaction in the present study, the radiation drag would extract angular momentum from the disk. However, we here stress that our results do not change very much even if we take the radiation drag into consideration. Miller & Lamb (1993) have reported that the mass accretion is enhanced via radiation drag by the radiation from the NSs. The radiation drag-induced mass-accretion rate is given by L_{NS}/c^2 , if all photons emitted at the NS surface contribute to extract the angular momentum (see also Umemura 2001). This value is much smaller than the resulting mass-accretion rate (see Figure 4). Additionally, the radiation drag-induced mass-accretion rate by the radiation from the disk is L_{rad}/c^2 maximum. It is also smaller than our results as shown in Figure 4. Since photons are emitted from rapidly rotating matter, and since some part of the photons escape through the rarefied region above the disk without any interaction with the disk matter, the efficiency of the radiation drag would decrease. Thus, we conclude that our present results do not change very much due to radiation drag. For a detailed study, we should self-consistently solve the radiation fields and the accretion flow, by performing the relativistic RHD simulations.

5. CONCLUSIONS

By performing two-dimensional RHD simulations, we investigated the supercritical accretion flows around the NSs. We summarize our results as follows.

(1) Since the radiation energy, as well as the gas energy, is not swallowed by the NS, and since the rotation energy is effectively converted to radiation energy at the innermost regions via the viscosity, the radiation force is enhanced near the NS surface. The enhanced radiation force

counteracts with the gravity and produces high-density regions around the NSs. Such a high-density shell is a peculiar structure of supercritical accretion flows onto the NSs, although the disk and outflows are also produced in the case of the BH accretion flows.

(2) Although the enhanced radiation force reduces the mass-accretion rate, and drives the strong outflows above and below the disk, supercritical disk accretion onto the NS is possible. The mass-accretion rate onto the NS is 20–30% of that onto the BH, on the condition that we employ the same mass-input rate. The mass-outflow rate is a few-times larger in the NS accretion flows than in the BH accretion flows.

(3) The accreting matter releases most of its energy before reaching the NS surface. Due to this mechanism, the luminosity of the NS is insensitive to the mass-accretion rate. Therefore, although the matter accretes onto the NS at the supercritical rate, the radiation force does not exceed the gravity at the NS surface.

(4) The supercritical accretion flows onto the NSs mainly release the accretion energy as the kinetic energy of the outflows, especially for a large mass-accretion rate. In contrast, the kinetic energy output rate via the outflows does not exceed the disk luminosity in the case of BH accretion flows.

(5) Our simulations succeed in reproducing the observed properties of the SS433 jets, except for the collimation angle. The resulting jet velocity ($0.2 - 0.3c$) and mass-outflow rate ($150 - 700L_E/c^2$) agree with the observations. However, the collimation angle of the jet in our simulations ($\sim 20^\circ$) is larger than that of SS433 (a few degrees).

We would like to thank the an anonymous reviewer for many helpful comments. We especially thank N. Shibasaki, H. Susa, H. Takahashi, S. Mineshige, Y. Kato, and T. Harada for useful comments and discussions. The calculations were carried out by a parallel computer at Rikkyo University and Institute of Natural Science, Senshu University. This work is supported in part by a special postdoctoral researchers program in RIKEN. We acknowledge a research grant from Japan Society for the Promotion of Science (17740111).

References

Abramowicz, M. A., Czerny, B., Lasota, J. P., & Szuszkiewicz, E. 1988, *ApJ*, 332, 646

Backer, D. C., Kulkarni, S. R., Heiles, C., Davis, M. M., & Goss, W. M. 1982, *Nature*, 300, 615

Balbus, S. A. 2003, *ARA&A*, 41, 555

Bhattacharyya, S., Bhattacharya, D., & Thampan, A. V. 2001a, *MNRAS*, 325, 989

Bhattacharyya, S., Misra, R., & Thampan, A. V. 2001b, *ApJ*, 550, 841

Bhattacharyya, S., Thampan, A. V., Misra, R., & Datta, B. 2000, *ApJ*, 542, 473

Burger, H. L. & Katz, J. I. 1980, *ApJ*, 236, 921

Burger, H. L. & Katz, J. I. 1983, *ApJ*, 265, 393

Demmel, V., Morfill, G., & Atmanspacher, H. 1990, *ApJ*, 354, 616

Eggum, G. E., Coroniti, F. V., & Katz, J. I. 1988, *ApJ*, 330, 142

Hawley, J. F., Balbus, S. A. & Stone, J. M. 2001, *ApJ*, 554, L49

Hayashi, C., Hoshi, R., & Sugimoto, D. 1962,

Inoue, H., Shibasaki, N., & Hoshi, R. 2001, *PASJ*, 53, 127

Kato, Y., Hayashi, M. R., & Matsumoto, R. 2004, *ApJ*, 600, 338

Kato, Y., Hayashi, M. R., Miyaji, S., & Matsumoto, R. 2001, *Advances in Space Research*, 28, 505

Klein, R. I., Chevalier, R. A., & Stockman, H. S. 1980, *ApJ*, 237, 912

Koldoba, A. V., Lovelace, R. V. E., Ustyugova, G. V., & Romanova, M. M. 2002, *AJ*, 123, 2019

Kotani, T., Kawai, N., Matsuoka, M., & Brinkmann, W. 1996, *PASJ*, 48, 619

Levermore, C. D. & Pomraning, G. C. 1981, *ApJ*, 248, L321

Lipunov, V. M. 1982, *AZh*, 59, 87

Machida, M., Matsumoto, R., & Mineshige, S. 2001, *PASJ*, 53, L1

Miller, G. S. 1990, *ApJ*, 356, 572

Miller, M. C., & Lamb, F. K. 1993, *ApJL*, 413, L43

Ohsuga, K. 2006, *ApJ*, 640, 923

Ohsuga, K., Mineshige, S., & Watarai, K. 2003, *ApJ*, 596, 429

Ohsuga, K., Mori, M., Nakamoto, T., & Mineshige, S. 2005, *ApJ*, 628, 368 (Paper I)

Okuda, T. 2002, *PASJ*, 54, 253

Okuda, T., & Fujita, M. 2000, *PASJ*, 52, L5

Paczynsky, B. & Wiita, P. J. 1980, *A&A*, 88, 23

Romanova, M. M., Ustyugova, G. V., Koldoba, A. V., Wick, J. V., & Lovelace, R. V. E. 2003, *ApJ*, 595, 1009

Rybicki, G. B. & Lightman, A. P. 1979, *Radiative Processes in Astrophysics* (New York: John Wiley & Sons, Inc.)

Shakura, N. I. & Sunyaev, R. A. 1973, *A&A*, 24, 337

Takahashi, H., & Makishima, K. 2006, *ESA SP-604: The X-ray Universe* 2005, 309

Turner, N. J. 2004, *ApJL*, 605, L45

Turner, N. J., Stone, J. M., Krolik, J. H., & Sano, T. 2003, *ApJ*, 593, 992

Umemura, M. 2001, *ApJ*, 560, L29

Wijnands, R., & van der Klis, M. 1998, *Nature*, 394, 344